GEOPHYSICS, VOL. 78, NO. 1 (JANUARY-FEBRUARY 2013); P. U1–U8, 7 FIGS.
10.1190/GEO2012-0071.1

Tracking of velocity variations at depth in the presence of surface velocity fluctuations

Benoit de Cacqueray[1], Philippe Roux[2], Michel Campillo[2], and Stefan Catheline[3]

ABSTRACT

We tested a small-scale experiment that is dedicated to the study of the wave separation algorithm and to the velocity variations monitoring problem itself. It handles the case in which velocity variations at depth are hidden by near-surface velocity fluctuations. Using an acquisition system that combines an array of sources and an array of receivers, coupled with controlled velocity variations, we tested the ability of beam-forming techniques to track velocity variations separately for body waves and surface waves. After wave separation through double beam forming, the arrival time variations of the different waves were measured through the phase difference between the extracted wavelets. Finally, a method was tested to estimate near-surface velocity variations using surface waves or shallow reflection and compute a correction to isolate target velocity variations at depth.

INTRODUCTION

Over the last 20 years, significant efforts have been made in earthquake seismology and seismic exploration to track and monitor subsurface velocity variations. Although seismological monitoring investigations have focused mainly on the coda of the records, seismic exploration monitoring has preferred to use body waves. The latter has also enjoyed renewed interest with the development of so-called 4D exploration, or reservoir monitoring, in which the result is spatially localized within the volume of interest. In this context, one of the main challenges is to separate the measure of the velocity variations at depth that are linked with the reservoir evolution from undesired velocity fluctuations due to surface variations induced by weather conditions and seasons.

Field tests that are designed to improve acquisition and processing techniques are time-consuming and generally costly. Although much less expensive, synthetic modeling suffers from insufficient representation of the wave propagation complexity. In this context, laboratory-scale experiments offer a powerful trade-off.

In seismology, the doublet method (Poupinet et al., 1984) was traditionally used to compute small relative velocity changes (dV/V) from multiple seismic events, and to perform accurate monitoring. More recently, coda wave interferometry (Snieder et al., 2002) has been used to monitor velocity variations using the coda of the noise-correlated records (Sens-Schönfelder and Wegler, 2006; Wegler and Sens-Schönfelder, 2007). Weak dV/V (of the order of 0.1%) have been observed after major seismic events or volcano eruptions, with continuous monitoring (Brenguier et al., 2008a, 2008b). Today, high-resolution processing techniques allow the temporal resolution of velocity changes to be reduced to about one day (Hadziioannou et al., 2011). At the same time, in seismic exploration, the need for reservoir monitoring to increase oil production has led to similar studies with the use of active sources. However, to date, reservoir monitoring algorithms have mainly been performed from ballistic arrivals, as they provide accurate identification of arrivals that are reflected off the target area at depth.

In the 4D seismic exploration field, repeatability of the active source and separation of the recorded reflections are the main issues. The "cross equalization" technique is one conventional method for handling these difficulties (Ross et al., 1996). Considering several stacks of traces acquired from the same area but at different times, cross equalization consists in matching the wavelets corresponding to the subsurface events in phase and amplitude. This is made difficult because of the (relatively large) static fluctuations that occur at the near surface that potentially hide any variations at depth. It also shows bias when several wave arrivals are superimposed in the time-gated wavelets. This method generally relies on the common depth point stacking of collections of traces to obtain an unambiguous estimation of the useful wavelets. However, extra

Manuscript received by the Editor 28 February 2012; revised manuscript received 6 July 2012; published online 11 December 2012.
[1]CGGVeritas: Land, Massy, France. E-mail: benoit.de.cacqueray@cggveritas.com.
[2]University Joseph Fourier, ISTerre, Grenoble, France. E-mail: Philippe.Roux@ujf-grenoble.fr; Michel.Campillo@ujf-grenoble.fr.
[3]INSERM, Lyon, France. E-mail: stefan.catheline@inserm.fr.

care is required for raypath differences. Meunier et al. (1997) propose the use of surface-consistent corrections before stacking to handle this issue. Some improvements have been made to this cross equalization technique to reduce potential bias, as Rickett and Lumley (1998) introduce. Although conventional 4D exploration means redeploying a survey, a solution consists in burying the receivers and/or the sources permanently to handle the near-surface variations. Continuous 4D monitoring then becomes possible, as has been demonstrated by Forgues et al. (2011). The so-called virtual source method (with receivers buried below the complex overburden; see Bakulin and Calvert, 2006) shows good results leveraging on the advantages of the technique: (a) only a velocity model at depth is necessary and (b) the energy coming from above the receivers can be removed.

Practically, traveltime fluctuation compensation still faces important issues in land acquisition, which are sometimes impossible to solve. These include:

- In conventional 4D exploration, the time window used to compute the cross-equalization correction might contain several wave arrivals with different time-evolving variations.
- The cross-equalization correction requires a reliable velocity model to perform the so-called normal moveout correction used in seismic exploration.
- With buried sources, some records still include reflections at the free-surface (so-called ghosts), and these fluctuations can hide velocity variations at depth.
- The virtual source method requires burying receivers below the overburden.

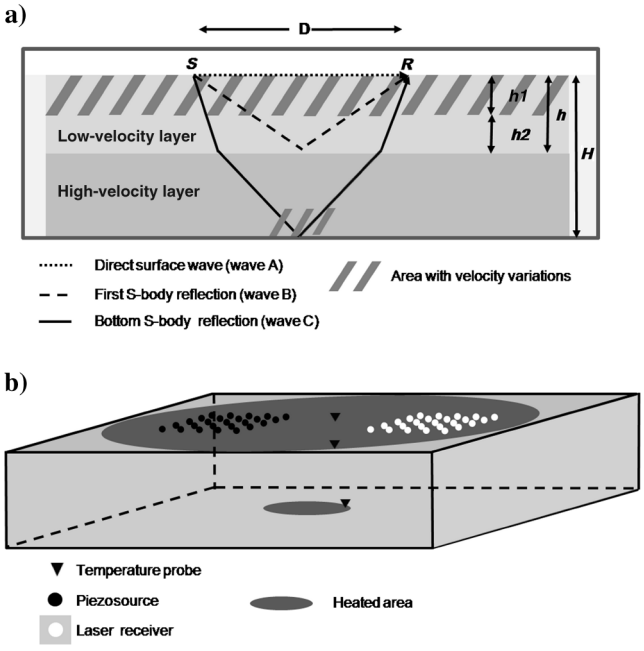

Figure 1. (a) Experimental environment of two agar-agar gel layers for a total volume of 450 × 450 × 150 mm. The two layers have the same width but different agar-agar volumetric concentrations, leading to different shear-wave velocities. The source-receiver system comprises a 12-mm-diameter piezosource emitting a 100 to 850 Hz linear chirp and a laser vibrometer recording the velocity vertical component at a 10-kHz sampling period. Shear and Rayleigh waves propagate along different paths (dotted, dashed, and solid lines) and interfere at the recording point. The $h1$ layer (dark gray) is affected by temperature variations at the surface. (b) Black and white spots at the gel surface represent the 5 × 5 source-receiver squared arrays used to process the beam-to-beam acquisitions. The black triangles are the three temperature probes: at the surface, 3 cm in depth, and at the bottom, which continuously monitor the temperature variations while the top surface and/or the bottom of the gel is heated (dark gray areas).

Time-delay corrections have also been proposed in marine acquisition, to cancel out the water layer variations between two surveys performed in the same area (McKay et al., 2003). These "indirect methods" also use one reflection (the water-bottom reflection) to correct the delays of another reflection. In this context, the incidence angle of the corrected wavelet is used to compute a correction in relation to a reference zero-offset reflection. However, several hypotheses (such as smooth velocity variations) are made and some a-priori knowledge is necessary, such as a robust and accurate water-bottom model. For 4D monitoring, a solution is to install a permanent seismic array using ocean bottom cables as done for the Valhall field in 2003 for time-lapse surveys acquired from September 2003 until April 2005 (Barkved et al., 2005).

In the present study, a new method is proposed, which consists of the combination of two ideas: (1) the use of beam-forming techniques on the source and receiver to extract the desired waves with an enhanced signal-to-noise ratio (S/N) and (2) the computation of a correction coefficient that links the temporal variations of different body- or direct-surface waves.

EXPERIMENTAL ENVIRONMENT

The propagation medium is a viscoelastic gel made from a high-concentration of agar-agar powder (4% to 6%) diluted in water. To monitor velocity variations in a laboratory context, we specifically designed a two-layer agar-agar gel in which shear body waves propagate at velocities around 10 m/s. The experimental environment is illustrated in Figure 1. In an aquarium that contains a volume of 450 × 450 × 150 mm agar-agar gel, shear body waves and surface waves can propagate and interfere (Figure 1a). The waves are emitted at point S and recorded at point R, which are separated by a constant offset $D = 18$ cm. The emitter is a 12-mm-diameter piezoelectric source fastened at the gel surface, which emits a chirp that ranges from 120 to 850 Hz. The receiver is an Ometron VQ-500 laser vibrometer that records the vertical component of the gel velocity with a 10-kHz sampling period. At frequencies of around 500 Hz, P waves are not excited due to their very large wavelength with respect to the gel size (the wavelength λ is about 3 m for a velocity of 1500 m/s). With an agar-agar concentration of 4% for the upper layer, the S-wave velocity is close to the Rayleigh wave velocity, at around 7.8 m/s. In the second layer, a greater agar-agar concentration of 6% gives an S-wave velocity of around 10.6 m/s.

In this environment, we assume that only the top part of the upper layer (Figure 1a, $h1$) is affected by the velocity fluctuations linked with the slowly evolving environmental conditions (mainly temperature and water content). Intense temperature fluctuations of short durations are generated at both of the gel surfaces. A heater is used above the top gel surface to generate homogeneous near-surface temperature variations, while a small resistor fastened to the bottom interface of the aquarium generates local temperature variations at depth. When the near-surface velocity variations,

which are referred to as dV, are strong, they typically hide the velocity variations at depth. The goal of the method here is to recover these velocity variations at depth independently of the surface fluctuations.

RELATIVE TIME FLUCTUATIONS WITH POINT-TO-POINT ACQUISITIONS

A test was performed with a repetitive single source-single receiver experiment between the central element of the source array and the central element of the receiver array. Because the temperature is not stabilized in the room, the gel faces fluctuations in day and night temperature. The recordings were repeated every 20 min, for a total acquisition period of 2.5 days. Figure 2a shows two single source-single receiver gel responses acquired a few hours apart after correlation of the received signal by the emitted chirp. Despite the obvious superposition of the shear and surface waves, it might still be possible to separate the relative temporal variations, dt/t, for the three dominant raypaths drawn in Figure 1a. A separate polarization study using 2C measurements confirmed that wave A is a Rayleigh wave and waves B and C are S-waves. However, as seen in Figure 2b, the temporal variations of these three wavelets are clearly interdependent, which makes it difficult to separate surface effects from velocity perturbations at depth.

As usually observed in seismic exploration investigations, this laboratory-scale experiment faces two major issues: (1) the dt/t computation is very sensitive to low S/N, as observed from the erratic evolution of the bottom-reflected lower-amplitude wave after day two and (2) despite the large frequency bandwidth of the chirp source, the small thickness of the upper layer results in wave mixing and superposition at the surface receiver and shear waves propagating in the gel (waves A and B in this experiment; Figure 1a). Wave interference prevents clear and separate detection of the temperature fluctuations for each wave.

This single source-single receiver experiment confirms that improvements must be made to the S/N of the recorded signals and to the processing allowed for efficient wave separation. We propose to apply array processing techniques through a combination of two source-receiver arrays that will resolve these issues.

ARRAY PROCESSING PERFORMED WITH DOUBLE BEAM FORMING

Beam forming (also known as time-delay beam forming) consists of the application of a time delay to each receiver according to the arrival angle, to perform constructive interference of the recorded signal on the whole array. With a 1D array, beam forming allows the separation of the incident waves with respect to their slowness (Figure 3a and 3b). Beam forming transforms the data from the time-offset domain to the time-slowness or time-angle domain. The aim of this transformation is to lead to a compact wave representation. The use of a 2D array provides further azimuth resolution, and thus better wave separation. The double beam forming (DBF) method consists of using beam forming on a source and a receiver array (Figure 3c). It combines two advantages of strong interest in seismic exploration. The first advantage is that, according to Huygen's principle, planar wavefronts are formed at the source array. It then becomes possible to use beam forming at the receiver with shorter source-receiver distance. The second advantage is to separate the different waves with respect to five parameters: arrival time, source slowness, receiver slowness, source azimuth, and receiver azimuth (Krüger et al., 1993, 1996; Roux et al., 2008). The DBF method has already been demonstrated in a geophysics context, with 2D source-receiver arrays using laboratory-scale data (de Cacqueray et al., 2011). As well as wave separation, DBF also provides significant array gain, which increases the S/N of the processed data. Using two arrays of $N = 5 \times 5 = 25$ receivers for receiving and $M = 5 \times 5 = 25$ sources for the emission (Figure 1b), and in the case of additive Gaussian noise, the expected S/N gain after DBF is $\sqrt{NM}$ (Benesty et al., 2008).

As the point source S and the point receiver R are replaced by a source array and a receiver array, the experimental configuration in Figure 1a is transformed into the experimental configuration described in Figure 1b. To automatically sample the receiver array points, a remotely controlled mirror was used above the gel to modify the laser incidence angle. On the source side, 25 piezoelectric sources were fastened to the gel, and the source was performed sequentially from each point source using a multiplexer. In addition, three temperature probes were added at different depths, to monitor the gel temperature variations (Figure 1b).

Finally, DBF computation leads to a five-dimension matrix $S(t, u_s, u_r, \phi_s, \phi_r)$ in which each wave is associated with an intensity maximum. The symbols (u_s, u_r) correspond to the source and receiver slowness and (Φ_s, Φ_r) correspond to the source and the receiver azimuth. The 5D matrix visualization is complex. In this experiment, we focus on the appropriate slowness representation. For a given triplet (t, u_s, u_r), we consider the maximum value for all the source and receiver azimuths. This reduces the dimension to 3D by considering

$$\tilde{S}(t, u_s, u_r) = \max_{\phi_s,\phi_r}[S(t, u_s, u_r, \phi_s, \phi_r)]. \quad (1)$$

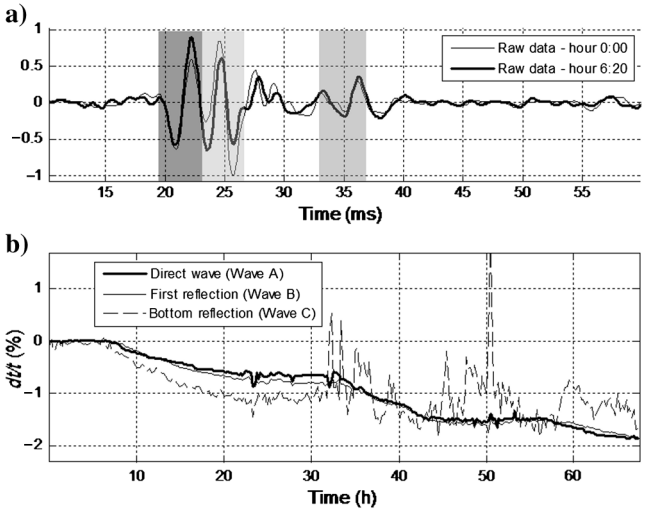

Figure 2. (a) Single source-single receiver signals after correlation by the emitted sweep and spherical divergence correction. Traces show high energy but mixed first-and second-arrivals around times of 25 and 27 ms (dark and light gray areas). The third wave (middle gray area) appears around time 37 ms out of a noise of comparable amplitude. (b) Relative arrival-time variations over the 2.5-day acquisition period. Bold line, direct surface wave; line, upper-layer shear wave reflection; dashed line, bottom reflection of the shear wave. The time between two successive acquisitions was about 20 min.

Considering the symmetry of the design, we assume $u_s \approx u_r = u$. Then the S function is transformed into a 2D function

$$\bar{S}(t,u) = \tilde{S}(t,u,u). \tag{2}$$

Figure 4b shows a representation of the $\bar{S}(t,u)$ envelope called a "vespagram" in seismology (Davies, 1971). This representation enables the display of the different waves in a single plot.

On the vespagram, the three waves described in Figure 1a (waves A, B, and C) are clearly visible around the times 25, 27, and 37 ms. Other 2D representations are possible by extracting 2D subsets of the function S. Figure 4c and 4e represents 2D views within this matrix in the "source azimuth/receiver azimuth" domain or the "source slowness/receiver slowness" domain (Figure 4f).

Wave extraction using DBF consists of zeroing the S matrix except for the intensity peak related to the wave(s) of interest. When the wave extraction is limited to the source array/receiver array centers (Cs and Cr), the DBF traces can directly be averaged in the angle domain over the intensity peak (Roux et al., 2008).

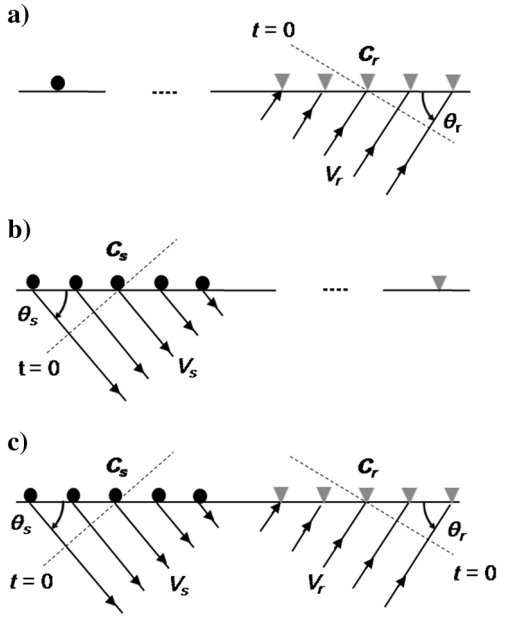

Figure 3. (a) Shown are the source (black circle), receivers (gray triangles), receiver array center (C_r), arrival angle (θ_r) in-phase plane for time reference (dashed line), and velocity (V_r) at the receiver array. By projecting the incident wavefronts on plane waves, the beam forming transforms the recorded data on the receiver array from the position domain to the angle domain, in such a way that the wavefield intensity is focused at certain elevation angles (represented by the angle θ_r). According to the relation $u_r = \cos\theta_r / V_r$, where u_r is the slowness, the beam forming is computed in the slowness domain. (b) Sources (black circles), receiver (gray triangle), receiver array center (C_s), in-phase plane for time reference (dashed line), and velocity (V_s) at the source array. According to the reciprocity theorem, beam forming can also be performed on the source array with respect to the reference point C_s. (c) When used simultaneously at the source and receiver arrays, the beam-forming process is called DBF. As planar wave fronts are formed at the source and receiver sides, DBF remains efficient even at short source-receiver distances. DBF provides the selection of waves with respect to their source and receiver slownesses. Extending the delay computation to 2D arrays also provides the azimuth information of the propagating waves. Modified from Krüger et al. (1996).

Figure 4g shows the DBF result for wave C, to be compared with Cs-to-Cr raw data (Figure 4a).

THEORETICAL RELATIVE VELOCITY VARIATIONS

The single source-single receiver results in Figure 2 show that the arrival-time fluctuations of the surface and shear waves are linked. The relative time variations (dt/t) of the three propagating waves appear more or less proportional, but not equal. This suggests that the dt/t computed for a given wave cannot be used directly to derive the dt/t of another wave. The analytical expression of the correction coefficient is further developed in the following paragraph.

In the present study, we only consider the near-surface velocity variations and the velocity variations at depth (and the corresponding traveltime variations). For each body wave, we have

$$\frac{dt_x}{t_x} = \frac{dt_{x,d}}{t_x} + \frac{dt_{x,ns}}{t_x}, \tag{3}$$

where the subscript d stands for depth, ns for near-surface, and x for wave B or C.

For the first layer of thickness h (see Figure 1a), we assume a near-surface velocity change dV (Figure 5a), for depths between 0 and $h1$ ($0 \le h_1 \le h$). At a given depth z, the velocity varies from $V(z)$ to $V(z) + \delta V(z)$. For an infinitesimal sublayer of thickness δz, the path length for wave x ($x = B$ or C) is $\delta s_x = \delta z/(\cos\theta_x)$ (Figure 5b).

Taking into account the velocity and incidence variations, the traveltime difference is then

$$\delta t_x(z) = \frac{\delta z}{\cos(\theta_x + \delta\theta_x)} \frac{1}{V(z) + dV(z)} - \frac{\delta z}{\cos\theta_x} \frac{1}{V(z)}. \tag{4}$$

According to Fermat's principle, a weak velocity variation does not modify the raypath to first order, which means that the elevation angle can be considered as constant:

$$\delta t_x(z) = \frac{\delta z}{\cos\theta_x} \frac{1}{V(z) + dV(z)} - \frac{\delta z}{\cos\theta_x} \frac{1}{V(z)}. \tag{5}$$

Assuming $dV(z) << V(z)$, we have

$$\delta t_x(z) \approx -\frac{\delta z}{\cos\theta_x} \frac{dV(z)}{V(z)^2}. \tag{6}$$

It then follows that

$$\delta t_C(z) = \delta t_B(z) \frac{\cos\theta_B}{\cos\theta_C}. \tag{7}$$

To obtain the complete traveltime delay over the first layer, we have to integrate the variation from 0 to h. As the velocity only varies between depth 0 and h_1, we obtain

$$dt_{C,ns} = \frac{1}{h_1}\int_0^{h_1} \delta t_C(z)\, dz = \frac{1}{h_1}\int_0^{h_1} \frac{\cos\theta_B}{\cos\theta_C}\delta t_B(z)\mathrm{d}z. \tag{8}$$

Neglecting incidence angle perturbations, we obtain a relationship that links the traveltime variations of waves B and C for the near-surface

$$dt_{C,ns} = \frac{\cos\theta_B}{\cos\theta_C}\frac{1}{h_1}\int_0^{h_1}\delta t_B(z)dz = \frac{\cos\theta_B}{\cos\theta_C}dt_{B,ns}. \quad (9)$$

This relationship can be rewritten with relative traveltime variations

$$\frac{dt_{C,ns}}{t_C} = \frac{t_B}{t_C}\frac{\cos\theta_B}{\cos\theta_C}\frac{dt_{B,ns}}{t_B}. \quad (10)$$

This means that by using equations 3 and 10, the traveltime variations of wave C at depth can be deduced using the near-surface traveltime variations of wave B

$$\frac{dt_{C,d}}{t_C} = \frac{dt_C}{t_C} - \frac{dt_{C,ns}}{t_C} = \frac{dt_C}{t_C} - \frac{t_B}{t_C}\frac{\cos\theta_B}{\cos\theta_C}\frac{dt_{B,ns}}{t_B}. \quad (11)$$

EXPERIMENTAL RESULTS

Using the above-mentioned laboratory-scaled configuration, we measure the time-evolving array-to-array response of the two-layer gel to monitor velocity variations created at the surface or at the bottom of the gel (Figure 1b).

To test the proposed time correction, we triggered two heaters at dedicated times. One heater was located at the upper surface to modify the near-surface velocity (Figure 6c, upper blue line), and the second heater was fastened to the aquarium below the gel to affect the gel velocity at depth (Figure 6c, lower red line). The temperature variation within the gel was recorded by three thermocouples placed at the surface, at the bottom, and in the middle of the upper layer (Figures 1b, 6a). We observed strong correlation

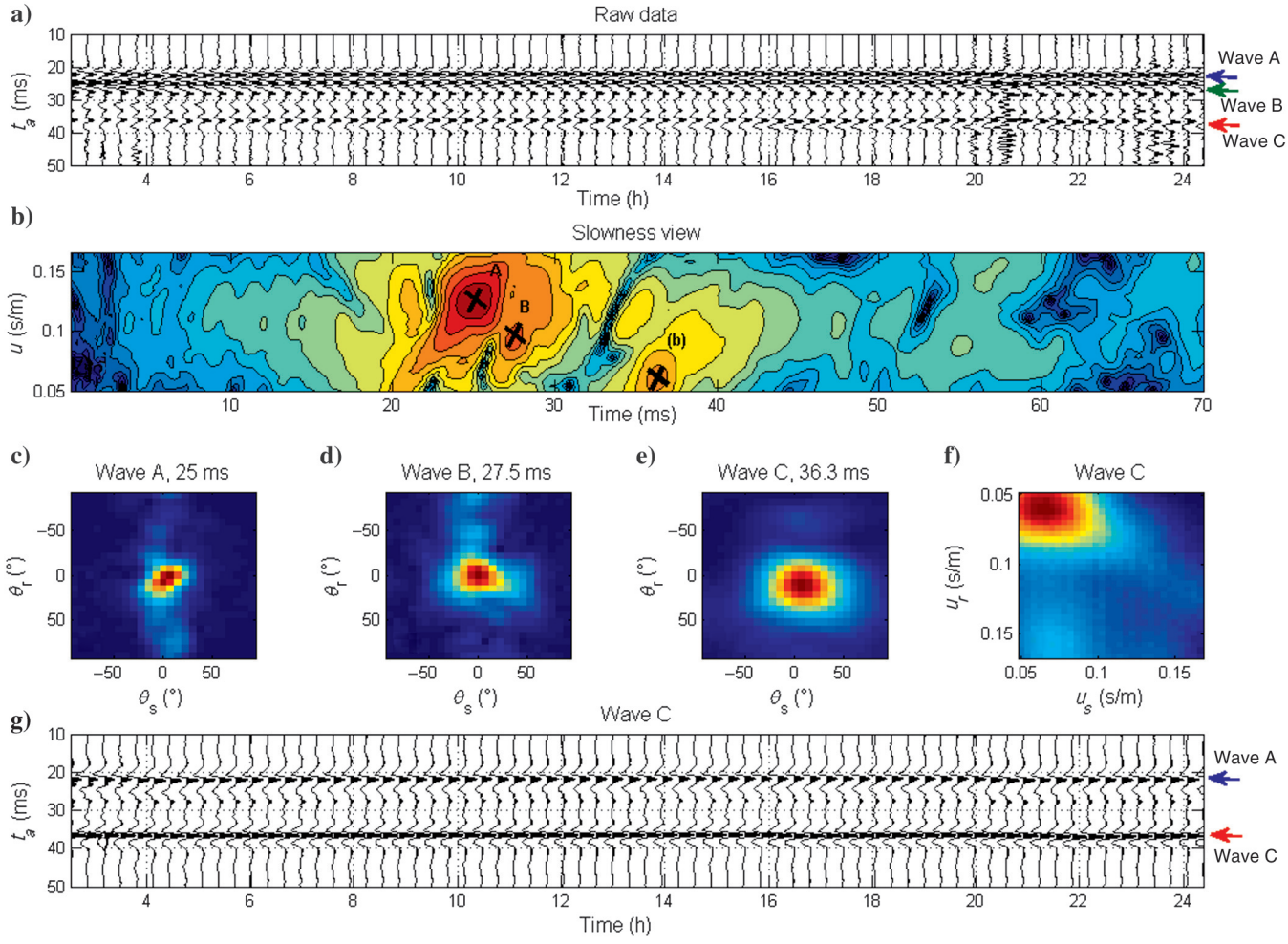

Figure 4. (a) Raw data for the C_s-to-C_r trace after normalization, where t_a is the acquisition time and t is the time of the experiment. Wavelets for waves A, B, and C are highlighted with blue, green, and red arrows, respectively, around the times 24, 27, and 37 ms. (b) Vespagram or 2D slowness view, after DBF. Waves A, B, and C intensity maxima are identified with black crosses and letters around time/slowness of (25 ms, 0.12 s/m), (27 ms, 0.09 s/m), and (37 ms, 0.06 s/m). (c-e) Waves A, B, and C intensity peaks in the source azimuth/receiver azimuth domain. (f) Wave C intensity peak in the source slowness/receiver slowness domain. (g) Wave C after DBF processing and normalization for $(u_s, u_r) = (0.066\ \text{s/m}, 0.062\ \text{s/m})$ and $(\Phi_r, \Phi_s) = (0°, 0°)$. Wave A (see blue arrow) is still visible but largely attenuated by the DBF processing when wave B is removed. Wave C (red arrow) can be isolated with time windowing. The time axes are the same as in (a).

between the temperature variations and activation of the heaters, taking into account that the bottom probe is slightly shifted from the heated area at depth. The temperature variations were kept within a range of 2.5°C to preserve the properties of the gel. In agar-agar gel with a concentration of 1.5% and 3%, Eude (2004) notes a reversible evolution in the gel properties (e.g., for S-wave velocity, or agar-agar density) for temperature variations of as low as 10°C.

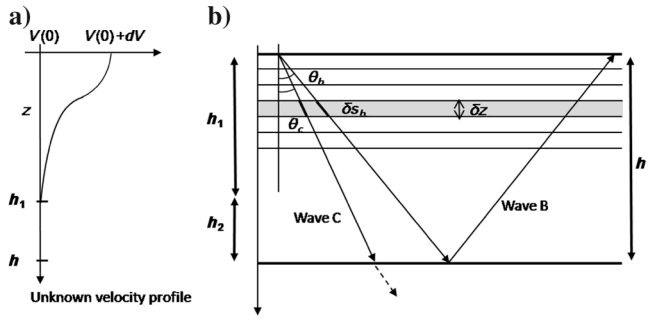

Figure 5. (a) Hypothetical velocity variation due to temperature and/or water content variations within the gel. The maximum velocity variation is assumed to be a few percent. (b) Display of the upper-layer reflected shear wave (wave B) and the bottom-reflected shear wave (wave C) propagating through the upper layer of the gel. The elevation angle for each wave is θ_B and θ_C. The upper gel layer faces near-surface velocity changes over a thickness $h1$. For small velocity variations at any sublayer of thickness δz and the raypath change can be neglected.

After extraction of waves A, B, and C using DBF, a time windowing is applied to the related wavelets. The S/N is larger than 26 dB for each wave, which is sufficient to correctly compute the relative time variation dt/t (Figure 6b). For each wave, the time variations dt were computed in two steps, with respect to a reference wavelet. The reference was obtained using the average of six traces in a quiet period between the times of 10 and 12 h. We first computed dt in the spectral domain by estimating the phase slope of each wavelet correlated by the reference. Then we refined the dt measurements in the time domain by minimizing the L2 norm of the difference between the current wavelet and the reference wavelet.

When the top heater was triggered at around 1 h, all of the waves were affected by the temperature variation, as each of them travels through the gel subsurface.

When the bottom heater was triggered, only wave C was affected, as seen around the time of 14 h (Figure 6b, bold line) highlighted with a black arrow. The gel heating caused a decrease in the shear velocity of wave C, and therefore a relative traveltime increase. After a relaxation time, the gel temperature returns to its initial value and the traveltime of wave C parallels this.

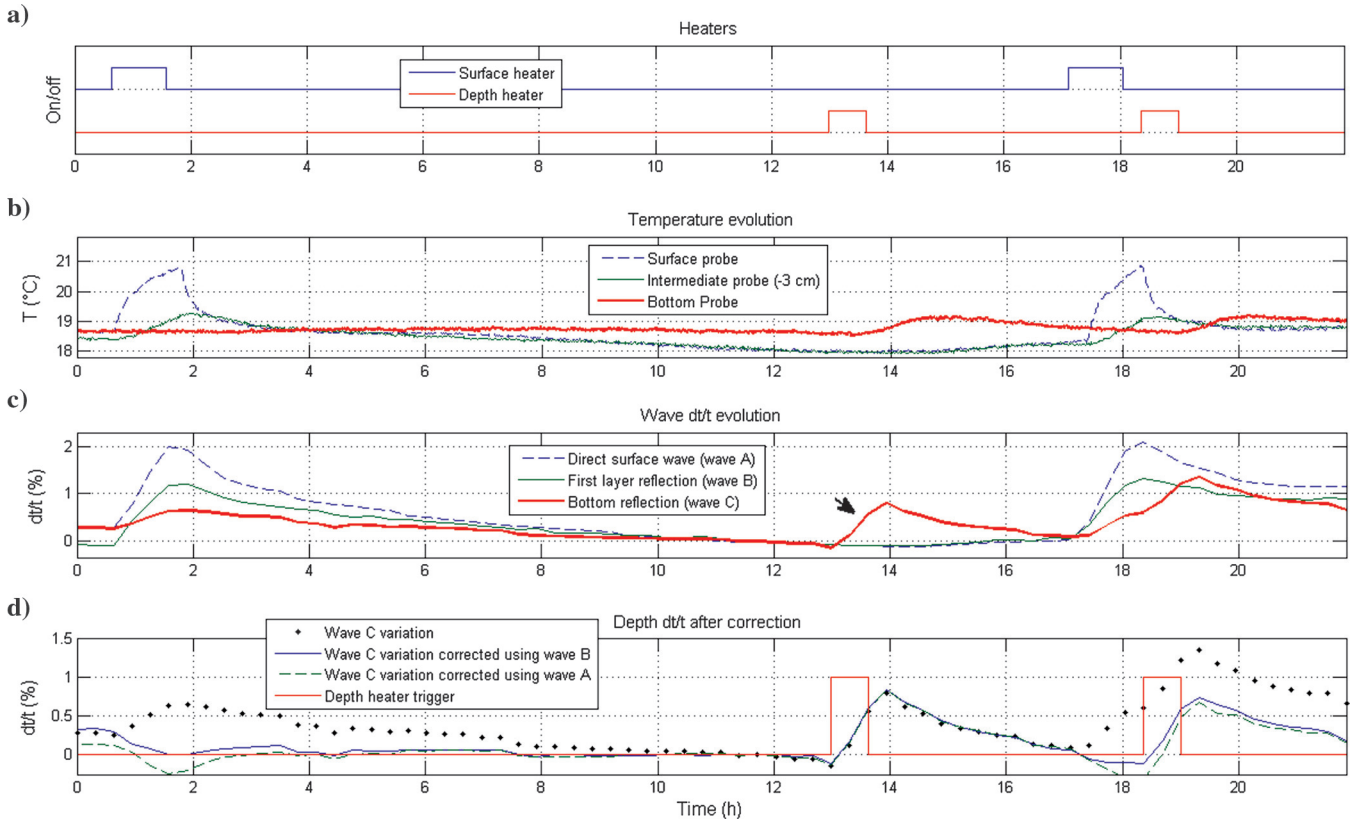

Figure 6. (a) Surface (blue) and bottom (red) heater triggers. When heating the upper layer of the gel (e.g., at 0.3 h), the three arrival times are affected as the three surface or body waves travel through this layer. When heating from the gel bottom (e.g., at 13 h), only the bottom reflection is affected by the gel velocity variation. When heating simultaneously from the surface and bottom heaters (at 17 to 19 h), a time variation is observed for the three waves, although it is not easy to differentiate this situation from the first one. (b) Temperature measurements at the three different depths: at the surface (dashed blue), in the middle of the upper layer (−3 cm depth, green), and at the bottom (−12.5 cm, bold red). (c) The dt/t computation for the three waves: direct surface wave (dashed blue), upper-layer shearwave reflection (green), and bottom-reflected shear wave reflection (bold red). (d) Bottom reflection traveltime variation (dotted black) without correction and after correction (blue) using the upper-layer shear wave reflection (red) and the direct surface wave.

In the third step, the surface heater was first triggered at around the time of 17 h, and then the bottom heater was activated at 18 h, before the complete relaxation of the gel surface temperature. Here, between 18 and 20 h, it is very difficult to discriminate between the traveltime variations caused by the surface and the bottom heaters (Figure 6b). In this case, the near-surface contribution observed for wave C can be removed using equation 11 thanks to the traveltime delays measured for wave B (Figure 6d, solid blue line) and the measured incidence angles (31.5° and 29.5°). The traveltime variations caused by the bottom heater only can then be isolated well.

We propose to go one step further. If, for some reason, no body wave is available to evaluate the near-surface variations, the traveltime correction can be made directly from the surface wave perturbations. This can be envisioned if the traveltime variations of the bottom-reflected shear wave are proportional to the traveltime variations of the surface wave. To check this hypothesis, the dt/t of wave C are plotted as a function of the dt/t of wave A (Figure 7a).

The global picture does not show a global linear relation. However, different behaviors can be observed. When the deep heater alone is heating (Figure 7a, stars), only wave C varies. When it is operated at the same time as the surface heater (Figure 7a, circles), the behavior of wave C is uncorrelated with the behavior of waves A and B. Selecting the traveltime perturbations between the times of 5 and 13 h, in which only the near surface is affected by velocity fluctuations, we clearly identify a linear relationship between delays of surface and body waves (Figure 7a, triangles) with a best-fit slope r equal to 0.4.

To a first approximation, the traveltime correction associated with the surface wave traveltime fluctuations for wave C can be computed as

$$\frac{dt_{C,d}}{t_C} = \frac{dt_C}{t_C} - r\frac{dt_A}{t_A}. \tag{12}$$

Applying this time correction to the bottom-reflected shear-wave measurement gives good results (Figure 6d, dashed green line). The attraction of this empirical technique is to be data-dependent only. By computing the linear coefficient between "body wave versus surface wave" traveltime perturbations, the near-surface effects can be removed from any of the body wave traveltimes.

Comparing the "body wave versus body wave" and the "surface wave versus body wave" correction techniques, slight differences can be noted. These might be due to some imperfections in the acquisition and/or processing chain. Finally, we also compared the empirical correction technique described in equation 12 with the theoretical one obtained in equation 11. Selecting the time periods during which a linear relationship was visible between the "wave C versus wave B" traveltime variations, the best-fit slope r associated with the bold line in Figure 7b is 0.55. This value of r concurs well with the value $t_B/t_C\,(\cos\theta_B)/(\cos\theta_C) = 0.536$ that can be computed from equation 11, confirming that the empirical and analytical correction techniques are similar when applied to body waves.

DISCUSSION

As shown above, the empirical correction method does not require knowledge of the elevation angles θ for the waves considered. This leads to two advantages. First, in the case of a high S/N or after extensive stacking, the velocity variation compensation might work without the need for arrays when the wave arrivals are separated in time. Second, it is possible to use surface waves to compensate for the near-surface fluctuations for body waves. In the latter case, the velocity variations cannot be predicted from the simple analytical approach described here for body waves. The ratio between the surface wave velocity fluctuations and the body wave velocity fluctuations at the near surface is frequency dependent and varies with the depth-dependent velocity profile. With the empirical measurement of the correction coefficient r, we assume that the traveltime perturbations between wave C and wave A or B shows a linear dependence to first order, as shown in Figure 7b. Considering in-field data, this second technique may face difficulties when surface wave behavior becomes more complex, for example, in the presence of a layering subsurface leading to higher-order Rayleigh modes. Indeed, the computation of the correction coefficient is related to the surface wave penetration at depth. If the surface wave penetration is larger than the depth affected by velocity variations, the relation $dt_A/t_A = -dV/V$ is not verified, and a velocity model is necessary to compute the sensitivity (Aki and Richards, 1981). If the velocity model presented in Figure 5a is simplified and replaced by a two-layer velocity model, we obtain $dt_A/t_A = h_1/h\,dt_B/t_B$. Using the correction factors r obtained in the section labeled "Theoretical Relative Velocity Variations," we can derive the ratio of the relative traveltime variations for waves A and B at the near surface, which leads to the estimate of $h_1 = 0.4.h/0.55 \approx 4.5$ cm. With a frequency bandwidth ranging from 120 to 850 Hz, the surface wave penetration is of the same order of magnitude of the central wavelength $\lambda \approx 2$ cm, which is less than h_1.

Another important point is the sensitivity of the method to spatial velocity variations. Equations 10 and 11 apply for a given array assuming that the velocity is constant below the arrays. If the velocities are different at the source and receiver array locations

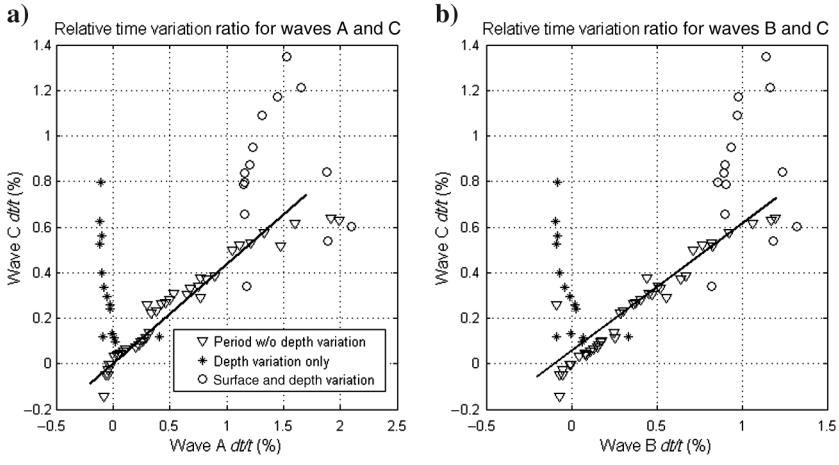

Figure 7. Plot of (a) "wave C versus wave A" traveltime variations and (b) "wave C versus wave B" traveltime variations during times when velocity variations occur at depth (stars), during times with near-surface variations (triangles), or during times with depth and surface variations (circles). The triangles confirm the linear relationship between the surface and shear waves for near-surface-induced traveltime perturbations.

inducing potential lateral refraction, the DBF intensity peaks may show up at different slownesses and/or azimuths for the source and receiver arrays ($u_s \neq u_r$ and $\phi_s \neq \phi_r$) but the wave extraction algorithm remains unchanged.

To study the case in which velocity varies within the arrays, it could be useful to investigate methods used in oceanography. For example, the turning-point filter is a modification of the plane-wave beam former, which compensates for the sound-speed variation along the array (Dzieciuch et al., 2001).

CONCLUSION

To conclude, we have experimentally studied at a laboratory scale the traveltime fluctuations of surface waves and shear body waves associated with temperature changes at the surface and at the bottom of a gel-based phantom. Using two source-receiver arrays and a DBF algorithm, the wave contributions can be identified and separated. This provides accurate measurements of traveltime perturbations, such that the velocity variations at depth can be monitored. In the case of spurious velocity variations that affect the near surface, two methods (one analytical and one empirical) can be proposed to account for the surface changes and to retrieve the velocity variations at depth only. In future investigations, the amplitude and/or slowness fluctuations will be studied in parallel with the traveltime changes and the frequency dependence of the correction coefficient r will be investigated. Application to real data would be performed in a further step.

ACKNOWLEDGMENTS

Benoit de Cacqueray was funded by CGGVeritas during this study.

REFERENCES

Aki, K., and P. Richards, 1981, Quantitative seismology: University Science Books.

Bakulin, A., and R. Calvert, 2006, Virtual source method: Overview of history and development: 76th Annual International Meeting, SEG, Expanded Abstracts, 2726–2730.

Barkved, O. I., K. Buer, T. G. Kristiansen, R. M. Kjelstadli, and J. H. Kommedal, 2005, Permanent seismic monitoring at the Valhall field, Norway, Presented at the International Petroleum Technology Conference, 10902-MS.

Benesty, J., J. Chen, and Y. Huang, 2008, Microphone array signal processing: Springer.

Brenguier, F., M. Campillo, C. Hadziioannou, N. Shapiro, R. M. Nadeau, and E. Larose, 2008, Postseismic relaxation along the San Andreas Fault at Parkfield from continuous seismological observations: Science, **321**, 1478–1481, doi: 10.1126/science.1160943.

Brenguier, F., N. M. Shapiro, M. Campillo, V. Ferrazzini, Z. Duputel, O. Coutant, and A. Nercessian, 2008, Towards forecasting volcanic eruptions using seismic noise: Nature Geoscience, **1**, 126–130, doi: 10.1038/ngeo104.

Davies, D., E. J. Kelly, and J. R. Filson, 1971, Vespa process for analysis of seismic signals: Nature Physical Science, **232**, 8–13, doi: 10.1038/physci232008a0.

de Cacqueray, B., P. Roux, M. Campillo, S. Catheline, and P. Boue, 2011, Elastic-wave identification and extraction through array processing: An experimental investigation at the laboratory scale: Journal of Applied Geophysics, **74**, 81–88. doi: 10.1016/j.jappgeo.2011.04.005.

Dzieciuch, M. A., P. F. Worcester, and W. H. Munk, 2001, Turning point filters: Analysis of sound propagation on a gyre-scale, Journal of the Acoustical Society of America, **110**, 135–149, doi: http://link.aip.org/link/doi/10.1121/1.1377869.

Eude, M., 2004, Etude expérimentale de la propagation d'une onde acoustique dans un milieu atténuant en présence d'hétérogénéité: Ph.D. thesis, University of Claude Bernard — Lyon I, pp. 144.

Forgues, E., E. Schissellé-Rebel, and J. Cotton, 2011, Simultaneous active/passive seismic monitoring of steam assisted heavy oil production: Presented at the 73rd Annual International Conference and Exhibition, EAGE.

Hadziioannou, C., E. Larose, A. Baig, P. Roux, and M. Campillo, 2011, Improving temporal resolution in ambient noise monitoring of seismic speed: Journal of Geophysical Research, **116**, B07304, doi: 10.1029/2011JB008200.

Krüger, F., M. Weber, F. Scherbaum, and J. Schlittenhardt, 1993, Double beam analysis of anomalies in the core mantle boundary region: Geophysical Research Letters, **20**, 1475–1478, doi: 10.1029/93GL01311.

Krüger, F., M. Weber, F. Scherbaum, and J. Schlittenhardt, 1996, Analysis of asymmetric multipathing with a generalization of the double-beam method: Bulletin of the Seismological Society of America, **86**, 737–749.

McKay, S., J. Fried, and C. Carvill, 2003, The impact of water-velocity variations on deepwater seismic data: The Leading Edge, **22**, 344–350, doi: 10.1190/1.1572088.

Meunier, J., F. Huguet, and J. M. Michel, 1997, Determining acquisition parameters time-lapse seismic recording: Presented at the 59th Annual International Conference and Exhibition, EAGE.

Poupinet, G., W. L. Ellsworth, and J. Frechet, 1984, Monitoring velocity variations in the crust using earthquake doublets: An application to the Calaveras Fault, California: Journal of Geophysical Research, **89**, 5719–5731, doi: 10.1029/JB089iB07p05719.

Rickett, J., and D. E. Lumley, 1998, A cross equalization processing flow for off-the-shelf 4D seismic data: 68th Annual International Meeting, SEG, Expanded Abstracts, 16–19.

Ross, C. P., G. B. Cunningham, and D. P. Weber, 1996, Inside the cross-equalization black box: The Leading Edge, **15**, 1233–1240, doi: 10.1190/1.1437231.

Roux, P., B. D. Cornuelle, W. A. Kuperman, and W. S. Hodgkiss, 2008, The structure of raylike arrivals in a shallow-water waveguide: Journal of the Acoustical Society of America, **124**, 3430–3439, doi: 10.1121/1.2996330.

Sens-Schönfelder, C., and U. Wegler, 2006, Passive image interferometry and seasonal variations of seismic velocities at Merapi Volcano, Indonesia: Geophysical Research Letters, **33**, L21302, doi: 10.1029/2006GL027797.

Snieder, R., A. Grêt, H. Douma, and J. Scales, 2002, Coda wave interferometry for estimating nonlinear behavior in seismic velocity: Science, **295**, 2253–2255, doi: 10.1126/science.1070015.

Wegler, U., and C. Sens-Schönfelder, 2007, Fault zone monitoring with passive image interferometry: Geophysical Journal International, **168**, 1029–1033, doi: 10.1111/gji.2007.168.issue-3.